CHEMISTRY OF MATERIALS

pubs.acs.org/cm

Article

Factors Governing the Chemical Stability of Shear-Exfoliated ZnSe(alkylamine) II−VI Layered Hybrids

Mengwen Yan, Sean M. Collins, Paul A. Midgley, and Jeremy I. Feldblyum*

Cite This: *Chem. Mater.* 2020, 32, 2379−2388

Read Online

ACCESS | Metrics & More | Article Recommendations | Supporting Information

ABSTRACT: Advances in the production of two-dimensional (2D) materials such as graphene and MoS_2 during the past two decades have spurred the search for other van der Waals materials with distinct functional properties. However, reducing the dimensionality of bulk van der Waals materials can lead to structural rearrangement and chemical degradation, especially in the presence of air. These challenges have slowed the progress of the discovery and analysis of chemically diverse 2D materials. Here, we provide a case study on the shear exfoliation of a class of wide band gap van der Waals materials termed II−VI layered hybrids (II−VI LHs) and show how reducing their dimension influences their structural and chemical stabilities. ZnSe(butylamine) and ZnSe(octylamine) are exfoliated, yielding shear-thinned material whose resistance toward degradation via oxidation is studied in depth by a variety of macro- and microscopic characterization techniques. Mechanical energy input, solvent−ligand interaction, and exposure to ambient conditions all play important roles in the stability of these materials. Our findings suggest that moderately coordinating alkylamine layers stabilize 2D materials that would otherwise degrade during exfoliation and exposure to air.

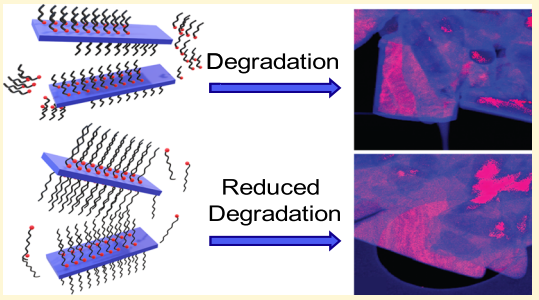

INTRODUCTION

Since the successful isolation and electrical characterization of graphene in 2004,[1] the number of known two-dimensional (2D) materials has grown rapidly. It is well established that the properties of 2D materials including transition-metal dichalcogenides,[2] h-BN,[3] phosphorene,[4] and metal halides[5] can differ significantly from those of their bulk counterparts. For example, MoS_2, an indirect band-gap semiconductor as a bulk material, possesses a direct band gap when isolated as a single 2D layer.[6] Among the large number of naturally occurring and chemically designed layered materials that can potentially be isolated as single layers, less attention has been given to the class of materials we refer to here as "II−VI layered hybrids" (II−VI LHs). II−VI LHs consist of 2D II−VI layers (typically formed from Zn or Cd and S, Se, or Te) bridged by mono- or ditopic amine ligands.[7] For instance, ZnSe(ba) (ba = *n*-butylamine), first reported in 2007 by the Li group,[8] consists of Zn and Se atoms bound to one another in a 1:1 ratio, generating inorganic slabs. These slabs are separated from one another by the alkylamine, which is bound to Zn via the N atom (Figure 1a). In this type of hybrid material, the adjacent layers are associated only via van der Waals forces between the alkyl chains, with no orbital interactions between the inorganic slabs. The demonstrated capability of II−VI LHs for broad-band white light emission,[9] potentially high charge carrier mobility,[10] and inclusion of a variety of cations[11] and ligands[12] have thus far been studied only in bulk powders or nanoparticles.[13−15] The properties of few- or single-layer II−VI LHs remain unexamined by experiment. Furthermore, incorporating II−VI LHs into thin film device architectures could be facilitated by their isolation as individual layers.

The exfoliation (delamination) of layered materials has undergone significant development to accommodate different material systems with the aim of improving exfoliation productivity while limiting damage to the exfoliated material. The Scotch-tape method, first used to obtain single-layer graphene,[1] and derivative techniques[16−18] can be used to acquire high-quality single-layer sheets. However, this approach suffers from a limited production rate. Higher production rates can be achieved by liquid exfoliation methods. Among liquid exfoliation methods including redox exfoliation,[19] intercalation,[20] ion exchange,[21] and sonication,[22] shear mixing (Figure 1b) is gaining attention as a scalable alternative to sonication that is capable of higher production rates.[23,24] Shear mixing was shown to make possible the exfoliation of large quantities of defect-free graphene and MoS_2,[24] while sonication has been reported to produce harsh conditions (high local pressure and rapid heating/cooling rates) that introduce defects in graphene.[17] Hybrid organic/inorganic materials, including II−VI LHs, represent a departure from

Received: November 20, 2019
Revised: February 15, 2020
Published: March 4, 2020

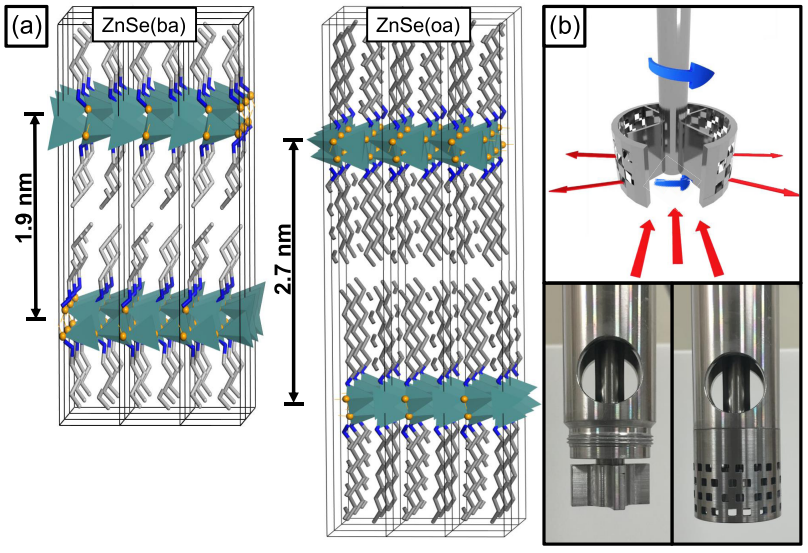

Figure 1. (a) Crystallographic model of ZnSe(ba) as reported in ref 8 and simulated model of ZnSe(oa) viewed along the crystallographic *b*-axis (Zn, teal polyhedra; Se, orange; N, blue; C, gray. H atoms omitted for clarity). (b) Schematic of shear mixer used for exfoliation of ZnSe(ba) and ZnSe(oa). The central rotor spins rapidly (up to 8000 rpm; blue arrows), leading to high shear rates ($>10^4$ s^{-1}) applied against the stationary outer screen (the stator). Mass flow is depicted by the red arrows: solution and solids are pulled up into the mixing head, after which they are pushed out through the 2 mm × 2 mm holes in the screen. Photographs of the rotor are shown without (bottom left) and with (bottom right) the stator attached.

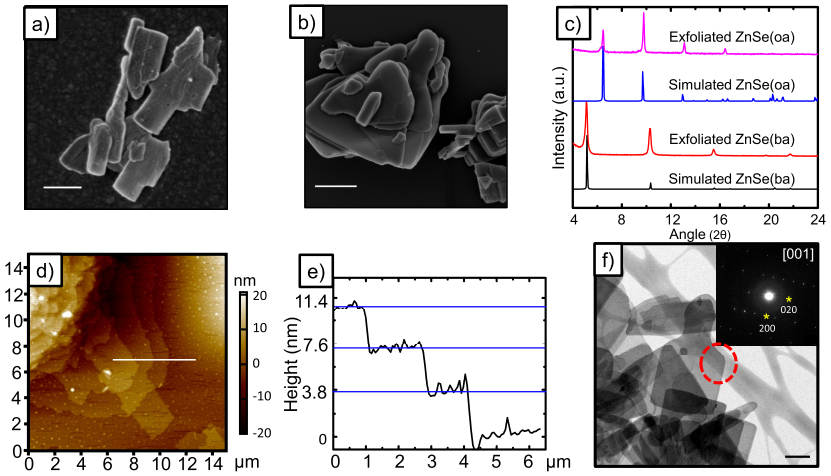

Figure 2. (a) SEM image of ZnSe(ba) after exfoliation in EtOH at a shear rate of 6000 rpm (scale bar: 1 μm). (b) SEM image of ZnSe(oa) after exfoliation in EtOH at a shear rate of 6000 rpm (scale bar: 1 μm). (c) Powder X-ray diffractograms of ZnSe(ba) and ZnSe(oa) after exfoliation in EtOH compared with diffractograms simulated from their respective structural models. (d) Atomic force microscopy (AFM) image of ZnSe(ba) exfoliated in EtOH. The white line corresponds to the step height measurement shown in panel (e). (e) Step height of multilayer flake shown in panel (d). Blue lines indicate intervals of 3.8 nm, corresponding to the calculated bilayer thickness of ZnSe(ba). (f) Transmission electron microscopy (TEM) image of ZnSe(ba) exfoliated in EtOH (scale bar: 500 nm) and corresponding selected area electron diffraction (SAED) (inset) viewed along the [001] zone axis in the region marked by a dashed red circle.

purely inorganic 2D materials. As such, to study the exfoliation of these materials for the first time, shear mixing was chosen here to potentially reduce the chemical and physical damage introduced by the exfoliation process.

Due to the weak out-of-plane van der Waals interactions between the amine-capped layers of II−VI LHs, we hypothesized that they could be exfoliated by mechanical means. This hypothesis motivates the examination of how exfoliation influences the morphological, structural, and chemical qualities of the resulting material, and whether shearing conditions and the choice of the bound alkylamine can affect these qualities as well.

In this work, we demonstrate the capabilities of shear mixing to exfoliate the archetypal layered hybrid ZnSe(ba)[8] and the newly synthesized ZnSe(oa) (oa = *n*-octylamine) and probe the interplay between exfoliation conditions and chemical and structural integrities of these layered hybrids. These materials were chosen based on their high crystallinity and reproducible synthesis in our laboratory. We show that shear exfoliation can produce II−VI LH dispersions having concentrations comparable to those achievable with shear-exfoliated graphene. Casting on substrates reveals shear-thinned sheets, the thinnest of which have thicknesses of just 4 nm, corresponding to bilayer ZnSe(alkylamine). Shear rate, exfoliation solvent, alkylamine identity, and environmental exposure all play

https://dx.doi.org/10.1021/acs.chemmater.9b04800
Chem. Mater. 2020, 32, 2379−2388

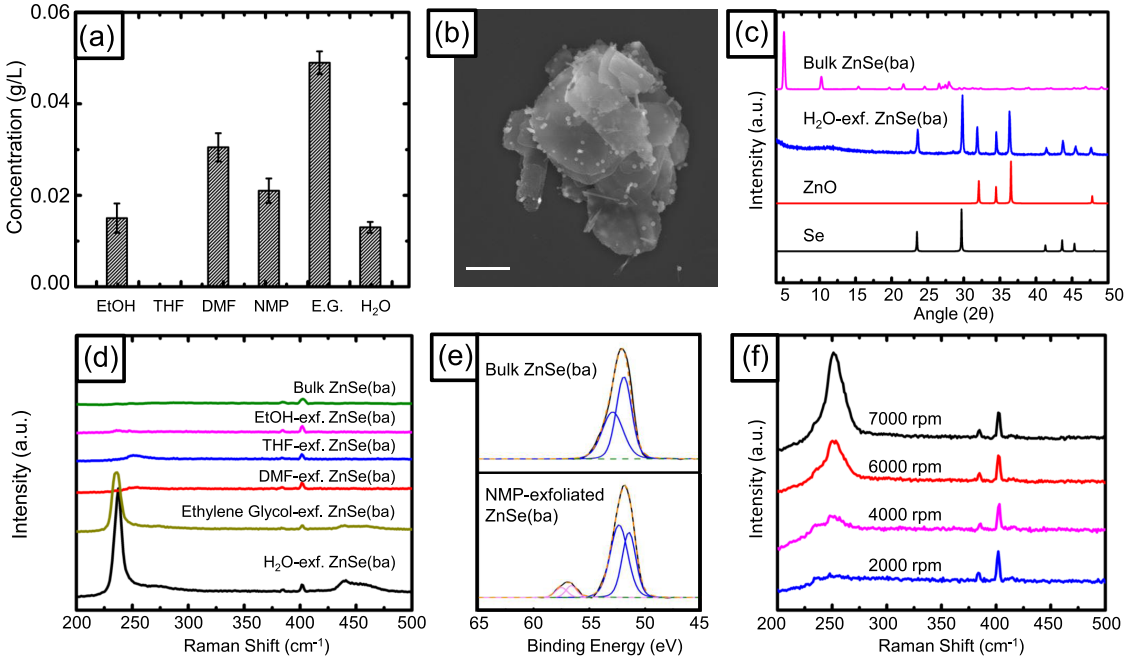

Figure 3. (a) Concentration of exfoliated ZnSe(ba) remaining in solution after shear mixing at 6000 rpm for 1 h and centrifugation at 1500 rpm for 40 min. (b) SEM image of ZnSe(ba) exfoliated in H_2O at 6000 rpm for 1 h (scale bar: 1 μm). (c) XRD pattern of ZnSe(ba) exfoliated in H_2O at 6000 rpm for 1 h compared with the XRD data of the as-synthesized bulk powder, ZnO,[32] and elemental Se.[33] (d) Raman spectra of ZnSe(ba) exfoliated in different solvents for 1 h at 6000 rpm. (e) X-ray photoelectron spectra of bulk ZnSe(ba) and ZnSe(ba) exfoliated in NMP at 6000 rpm for 1 h. Black lines indicate experimental data, dashed olive lines indicate fitted Shirley[37] backgrounds, dashed orange lines indicate fitting envelopes, and blue and pink lines indicate fitted peaks corresponding to ZnSe and Se, respectively. (f) Raman spectra of ZnSe(ba) exfoliated in NMP at different shear rates for 1 h.

important roles in the stability of the material. We elucidate factors governing LH stability and probe degradation at macro- and microscopic scales.

RESULTS AND DISCUSSION

To test the hypothesis that the layered structure of II−VI LHs renders them amenable to exfoliation in liquids, we subjected them to shear mixing (a process depicted schematically in Figure 1b). ZnSe(ba) was synthesized as described previously; ZnSe(oa) was synthesized by a ligand exchange procedure (see Materials and Methods). Subjecting them to shear mixing at 6000 rpm for 1 h in EtOH resulted in fine dispersions. After centrifugation to remove aggregated species, dispersions were deposited on silicon, dried, and analyzed by scanning electron microscopy (SEM). While bulk ZnSe(ba) appears as ∼5−15 μm diameter particles (Figure S1a), the layered structure of which is clearly visible at the particle edges, samples subject to shear exfoliation appear as qualitatively thinner sheets of lateral diameter typically less than 2 μm (Figure 2a). The smaller lateral diameter after exfoliation is attributed to the mechanical fracture of particles during shear mixing.[25] Similar observations were made for ZnSe(oa): larger particles prior to exfoliation (approximately 10 μm in diameter; Figure S1b) yield thinner sheets of reduced diameter (<2 μm) upon exfoliation (Figure 2b). Experimental powder X-ray diffraction (XRD) data of ZnSe(ba) and ZnSe(oa) after exfoliation in EtOH are shown with their corresponding simulated powder patterns in Figure 2c. Good agreement is found between the experimental and simulated powder patterns. Agreement is also found between the powder patterns of bulk and exfoliated powders (Figure S2). The lowest angle reflections (corresponding to the (002) and (004) crystallographic planes for ZnSe(ba) and ZnSe(oa), respectively) for ZnSe(ba) and ZnSe(oa) are 5.11 and 6.47° in 2θ, very close to those expected from crystallographic (ZnSe(ba)) and computed (ZnSe(oa)) models (5.17 and 6.47° in 2θ, respectively; Figure 1a). Hence, the averaged crystallographic integrity of these materials is preserved after shear mixing.

Having established that exfoliation of ZnSe(ba) and ZnSe(oa) is possible by shear mixing, the exfoliated flakes were further analyzed to quantify their thickness and diameter (Figure 2d−f). Figure 2d shows the tapping mode AFM data of ZnSe(ba) exfoliated in EtOH. The step heights measured on the surface of an 11 nm thick fragment fall between 3.6 and 3.8 nm (Figure 2e). Given that the interlayer spacing for ZnSe(ba) predicted from the crystallographic model is 1.9 nm,[8] these step heights correspond to those expected for bilayers. The thinnest flakes of exfoliated ZnSe(ba) we observed had thicknesses of 4.3 ± 0.1 nm (Figure S3a). This step height is 0.5 nm greater than that expected (3.8 nm) for a bilayer based on the crystallographic model. The cause of this discrepancy may be due to the presence of residual solvent trapped underneath the exfoliated ZnSe(ba), in analogy to greater-than-expected step heights commonly observed for single-layer graphene.[1] We emphasize that step heights between layers (rather than between the bottom layer and the substrate) are perfectly consistent with those expected for bilayer ZnSe(ba). Flake thicknesses varied, but those measured by AFM typically exhibited thicknesses below 20 nm. Representative examples are shown in Figures S4a−c and S5.

In the case of ZnSe(oa), step height measurements for a typical 1 μm diameter ZnSe(oa) flake (Figure S6a) exfoliated in EtOH at 6000 rpm for 1 h showed two different thicknesses (Figure S6b). One is 5 nm, in agreement with the predicted

https://dx.doi.org/10.1021/acs.chemmater.9b04800
Chem. Mater. 2020, 32, 2379−2388

bilayer thickness of ZnSe(oa). The other measured thickness falls between 3.8 and 4 nm. We tentatively attribute this height, which falls in between those expected for either a single layer (2.7 nm) or a bilayer (5.4 nm), to incomplete ligand exchange. The similarity in chemistry between ba and oa makes it challenging to distinguish between the two at nanometer scales. However, an incomplete exchange would allow additional oa ligand tilting, thereby reducing the thickness between inorganic layers, providing one explanation for some of the AFM step heights observed.

The layer thickness measurements recorded in AFM were further corroborated by step height analyses using information on the inelastic scattering probability observed in electron energy loss spectroscopy in scanning transmission electron microscope−electron energy loss spectroscopy (STEM−EELS),[26,27] showing a quantitative match to expected thickness differences for the structures of ZnSe(ba) and ZnSe(oa) (Figure S7).

Figure 2f presents transmission electron microscopy (TEM) imaging and selected area electron diffraction (SAED) data for ZnSe(ba) exfoliated in EtOH. After exfoliation in EtOH, ZnSe(ba) flakes exhibited a "cheeseboard" morphology, with a thinner protrusion extending from a rectangular body. ZnSe(oa) treated in the same manner showed a preference for a triangular morphology. Elemental analysis of flakes by X-ray energy-dispersive spectroscopy (EDS) confirmed the expected chemistry (Figure S8). SAED of ZnSe(ba) and ZnSe(oa) of the marked areas of the flakes in Figures 2f and S4c showed single-crystal diffraction patterns that match those expected from their respective crystallographic models (Figure S9). The planes of the flakes were perpendicular to the crystallographic *c*-axis, consistent with the contention that these materials exfoliate parallel to the plane of the inorganic layer. These data show that crystalline, few-layer sheets of ZnSe(ba) and ZnSe(oa) can be obtained by exfoliation from EtOH.

Given the efficacy with which ZnSe(ba) and ZnSe(oa) can be exfoliated in EtOH, we used ZnSe(ba) as the basis for testing additional solvents to examine potential differences in dispersion and flake characteristics. Exfoliation of ZnSe(ba) from EtOH, tetrahydrofuran (THF), *N*,*N*-dimethylformamide (DMF), *N*-methylpyrrolidone (NMP), ethylene glycol, and H_2O was performed by shear mixing at 6000 rpm for 1 h. These solvents were selected based on their differences in surface tension, a parameter that affects the free energy of solid−liquid interfaces[28] and which has proven to be a significant parameter in controlling the yield of 2D materials such as graphene and MoS_2 during shear exfoliation.[29−31] Suspensions of exfoliated ZnSe(ba) were subject to centrifugation at 1500 rpm for 40 min to remove poorly dispersed material, and the concentrations of the resultant dispersions were immediately determined by ultraviolet−visible (UV−vis) absorption spectroscopy. The measured concentrations of the dispersions are shown in Figure 3a and Table S1. With the exception of THF, which was unable to disperse measurable amounts of material, each solvent retained exfoliated ZnSe(ba) at concentrations between 13 and 50 mg/L. These values are comparable to those achieved for graphene, MoS_2, and other 2D materials under similar conditions.[24] Dispersion concentration is maximized with ethylene glycol; however, it must be noted that centrifugation removes more ZnSe(ba) from the supernatant for solvents with lower surface tension and density in accordance with Stokes' law (eq S1). Hence, the high retention of ZnSe(ba) in ethylene glycol is due at least in part to the relative ineffectiveness of centrifugation to remove larger aggregates. As noted previously by Hernandez et al.,[29] the absolute values of dispersion concentration could be further optimized by modifying processing conditions (exfoliation and centrifugation time and speed), but the dispersibilities relative to one another would not be expected to change.

As observed for exfoliation of ZnSe(ba) from EtOH, reductions in both lateral diameter and thickness were evident across the range of solvents tested. The minimum thicknesses obtained for ZnSe(ba) flakes exfoliated in DMF, NMP, and ethylene glycol fell between 4.1 and 4.3 nm (Figure S3b−d), suggesting bilayer material. We interpret these data, in combination with the data collected for EtOH-exfoliated ZnSe(ba), to indicate that the production of bilayer ZnSe(ba) from solution exfoliation may be favored. Alternatively, monolayer material may be produced, but degrades prior to sample analysis. The chemical degradation of ZnSe(ba) and ZnSe(oa) is discussed below.

Changes in morphology were evident depending on the solvent used for exfoliation (Figure S10). Most dramatically, exfoliation from H_2O led to the production of spheroid and rodlike particles in addition to the expected flat plates (Figures 3b and S10f). These particles were confirmed as elemental Se by EDS (Figure S8). Bulk ZnSe(ba) did not exhibit these features; spheroid particles were visible only to a minor extent in ZnSe(ba) exfoliated in other solvents. Furthermore, exfoliation from H_2O produced particles as thin as 2.8 ± 0.2 nm, a value inconsistent with that expected for monolayer or bilayer material (Figure S3e).

These morphological changes hint that ZnSe(ba) is sensitive to the conditions used for exfoliation. Accordingly, ZnSe(ba) exfoliated in H_2O was analyzed by XRD to determine whether the lamellar ZnSe(ba) structure is maintained (Figure 3c). A near-complete loss of reflections below 20° in 2θ occurred after exfoliation; however, numerous new, sharp reflections emerged at higher angles. These reflections matched those of ZnO[32] and elemental Se,[33] suggesting that exfoliation from H_2O transforms ZnSe(ba) into ZnO and Se.

To better understand potential chemical changes occurring in ZnSe(ba) due to exfoliation, Raman spectra and X-ray photoelectron spectra of the exfoliated material were obtained (Figure 3d,e). A variety of chemical changes were observed in the exfoliated sheets, depending on the solvent used for exfoliation. The material resulting from exfoliation from H_2O and ethylene glycol exhibited peaks consistent with the previously reported Raman shifts of h-Se nanowires[34] (prominent peaks at 236, 439, and 458 cm^{-1}), indicating that exfoliation from H_2O and ethylene glycol leads to the formation of elemental Se (Figures 3d and S11). Considering the XRD data discussed earlier (Figure 3c), ZnSe(ba) exfoliated in these solvents partially decomposes to form both Se and ZnO. Complete decomposition did not occur, as the XPS signature of ZnSe(ba) centered at 52.5 eV (blue lines) was still present (Figure S12e,f). However, broad peaks centered at 57.5 eV (pink lines) suggest partial transformation of ZnSe(ba) to Se due to exfoliation. Analysis of the Raman peaks of NMP-exfoliated ZnSe(ba) (Figure S13a) suggests the simultaneous formation of amorphous Se (251 cm^{-1}) and h-Se nanowires (236 cm^{-1}), further evidenced by peaks at binding energies of 56.5 and 57.5 eV[37] in the corresponding X-ray photoelectron spectrum (Figure 3d). Evidence of decomposition was less pronounced for ZnSe(ba) exfoliated in THF,

https://dx.doi.org/10.1021/acs.chemmater.9b04800
Chem. Mater. 2020, 32, 2379−2388

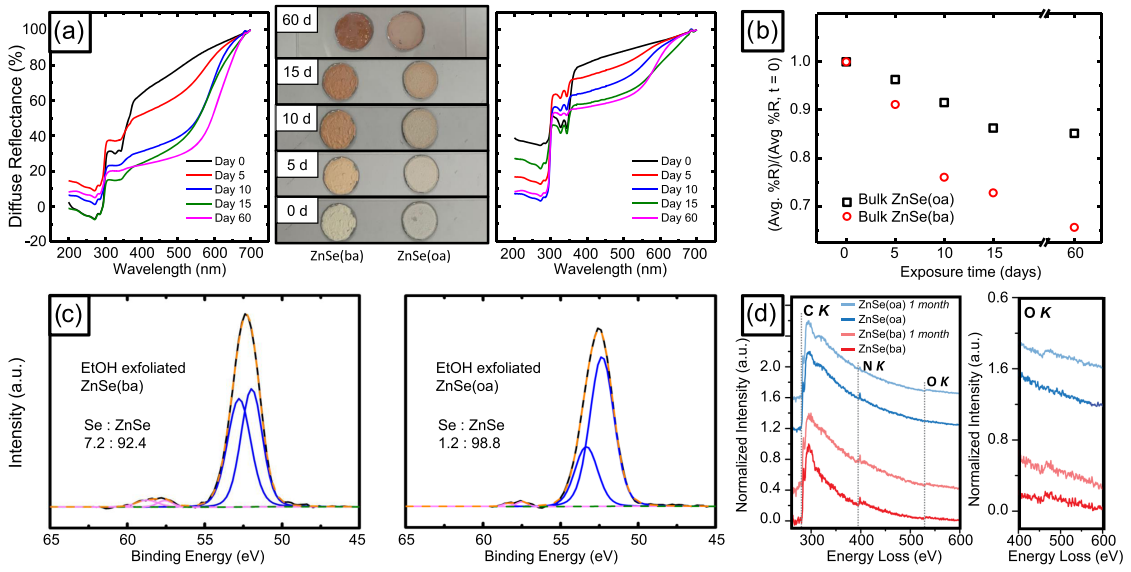

Figure 4. (a) Photographs and diffuse reflectance spectra of bulk (non-exfoliated) ZnSe(ba) and ZnSe(oa) powders left in ambient conditions over the course of 60 days. (b) Normalized average of diffuse reflectance in the visible region (400−700 nm) of ZnSe(ba) and ZnSe(oa) left in ambient conditions over a period of 60 days. (c) X-ray photoelectron spectra of ZnSe(ba) and ZnSe(oa) EtOH at 6000 rpm for 1 h. (d) Evaluation of oxidation over time for ZnSe(ba) (red) and ZnSe(oa) (blue) exfoliated in EtOH by electron energy loss spectroscopy, recorded <20 days after synthesis and after a further 1 month in air. Representative spectra across the C K, N K, and O K ionization edges are shown on the left. The right panel highlights spectra at the O K edge. The spectra are offset vertically for clarity. Additional spectra and positions on flakes are presented in Figures S15 and S16.

DMF, and EtOH; however, a broad peak of low intensity centered at 251 cm^{-1} was visible in the Raman spectra of these three samples (Figure 3d), consistent with the presence of some amorphous Se.[35,36] In addition, their X-ray photoelectron spectra indicated the presence of elemental Se in addition to that of ZnSe after exfoliation (Figure S12a−c; peaks near 57.5 eV). Although the collected XPS data are unable to distinguish between Zn in ZnSe and Zn in ZnO, we infer from the presence of elemental Se that oxidation of the layered material does occur to some extent (quantified in Table S2).

To test whether the degradation of exfoliated ZnSe(ba) can be mitigated by lowering the shear rate, ZnSe(ba) was exfoliated at different shear rates ranging from 7000 to 2000 rpm in NMP. NMP was chosen due to the clear and reproducible signatures of degradation in the corresponding Raman spectra of the processed material. Figure 3f shows the Raman spectra of these exfoliated samples. The influence of shear rate was apparent: the peaks at 236 and 251 cm^{-1}, corresponding to the presence of amorphous Se, reduced in intensity as shear rate was reduced. These results are quantified in Figure S13 and show that the energy input of shearing may be one of the factors affecting the degradation of samples during exfoliation. However, it should be noted that flakes exfoliated at 2000 rpm were approximately 2−4 times thicker than those exfoliated at 6000 rpm, as shown by AFM (Figure S4). Thus, the mitigated degradation may also be due to greater thickness of these exfoliated flakes.

Given the relative ease with which ZnSe(ba) degrades into Se and ZnO, we sought to better understand the impact of alkylamine chain length, exfoliation solvent, and time dependence on the microscopic manifestation of chemical and structural degradation. These parameters were selected with a view toward identifying key routes to the mitigation of degradation. For this purpose, the alkylamine chain length was varied by comparing ZnSe(ba) and ZnSe(oa). For solvent comparisons, EtOH was selected as an exfoliation solvent showing minimal degradation and NMP was selected as an exfoliation solvent showing higher rates of degradation. Comparing ZnSe(ba) and ZnSe(oa), the increased length of oa relative to that of ba was predicted to better prevent degradation, consistent with observations on other systems. For example, the oxidation of germanium nanowires can be better mitigated by functionalization with longer alkanethiols than with short ones.[38]

First, to better understand the intrinsic stabilities of ZnSe(ba) and ZnSe(oa) in air in the absence of exfoliation, bulk (non-exfoliated) ZnSe(ba) and ZnSe(oa) were exposed to ambient conditions over the course of 60 days. Color changes in both samples became apparent during this time (Figure 4a). ZnSe(ba) changed from an off-white to an orange-brown color after 10 days; after 60 days, the powder became completely brown. In contrast, similarly treated bulk ZnSe(oa) powder changed color more slowly; even after 60 days, the color did not reach the dark orange hue of its ba-containing analogue. These color changes were quantified by diffuse reflectance spectroscopy (DRS) (Figure 4a). The averages of the reflectance values in the visible region (400−700 nm), normalized to the first measured value (t = 0 days), are plotted in Figure 4b. A decrease of the average reflectance corresponds to the increasing absorbance of visible light. As expected based on visual observation, both ZnSe(ba) and ZnSe(oa) showed reduced reflectance of visible light over the course of the 60 day time series, suggesting increasing degradation. Notably, however, the reflectance of ZnSe(oa) decayed at a slower rate and appeared to stabilize at a significantly higher absolute value than did that of ZnSe(ba). Hence, at least prior to exfoliation, ZnSe(oa) is more stable than ZnSe(ba).

Further analysis by Raman spectroscopy (Figure S14) showed that these color changes corresponded to the

https://dx.doi.org/10.1021/acs.chemmater.9b04800
Chem. Mater. 2020, 32, 2379−2388

degradation observed previously in shear-exfoliated samples, that is, both samples exhibited signatures of elemental Se at 237 and 251 cm^{-1}. The decomposition products are different, however, in that ZnSe(ba) primarily produces amorphous Se (251 cm^{-1}), whereas ZnSe(oa) primarily produces crystalline Se (237 cm^{-1}). One explanation for this difference could be that the slower degradation of ZnSe(oa) provides time for crystallization to occur, unlike ZnSe(ba), where rapid degradation kinetically favors amorphous Se.

To examine the effect of air exposure on exfoliated samples, we then compared the Se 3d X-ray photoelectron spectra of ZnSe(ba) and ZnSe(oa) EtOH (Figure 4c). As determined by the ratio of integrated peak intensities of Zn-bound Se (binding energies of 52.8 and 51.9 eV, present in the II−VI LHs) to elemental Se (binding energies of 58.8 and 57.5 eV, indicating degradation), the extent of degradation is 6 times higher in ZnSe(ba) compared to that of ZnSe(oa). These results are consistent with the hypothesis that the longer oa ligands better stabilize the ZnSe layers of the parent material.

The ensemble characterization by XPS was complemented by local EELS analyses. Figure 4d presents EELS spectra of ZnSe(ba) and ZnSe(oa) shortly after exfoliation in EtOH and 1 month later, stored under ambient conditions. Carbon and nitrogen signatures were recorded as expected, with greater carbon signal (relative to the nitrogen signal) recorded from ZnSe(oa) samples due to the greater length of the surface-bound alkyl chains. Whereas oxygen was observed in the EELS spectra of all ZnSe(ba) flakes analyzed, several ZnSe(oa) flakes showed no measurable oxygen content. Oxygen was detected in the EELS spectra of flakes from all samples after storing them for 1 month in air, although the ZnSe(oa) sample showed lower oxygen content. Additional spectra and images from the corresponding areas are shown in Figure S15. Spectra for ZnSe(ba) and ZnSe(oa) exfoliated in NMP (Figure S16) showed detectable oxygen in all samples shortly after exfoliation, consistent with higher rates of degradation. An independent component analysis (ICA) map of ZnSe(ba) exfoliated in NMP revealed that the O K edge intensity is greatest in a conformal layer approximately 40−50 nm at the edge of the flakes (Figures S16 and S17). DRS, XPS, and EELS results together show that oxidation is a strong contributor to the degradation of these II−VI LHs in ambient conditions.

To test whether a correlation exists between the chemical degradation of these II−VI LHs and structural changes, scanning electron diffraction (SED) was used to analyze the crystalline flakes at the nanometer scale. X-ray diffraction of the exfoliated material and SAED, incorporating signal over hundreds of nanometers or more, are insensitive to local changes in crystal quality. SED instead uses an electron beam limited in diameter to <5 nm while maintaining a small beam convergence. The probe can then be used to acquire a "spot pattern" of Bragg scattering intensity at each probe position within a raster scan over a selected field of view. This variant of four-dimensional STEM ("4D-STEM") enables postacquisition data processing to obtain an image of the sample while simultaneously enabling analysis of diffraction patterns from each pixel in the real space image.[39,40] Figure 5 presents SED data from ZnSe(ba) and ZnSe(oa) flakes after exfoliation in EtOH. By selection of a subregion of a flake, the SED analogue of SAED allows precise local indexation of the observed crystal facets. ZnSe(ba) cheeseboard flakes exhibit (100) facets along the long edge (Figure 5b) with the orthogonal facet assigned as (010) (Figure S19b). ZnSe(oa) triangular flake facets were

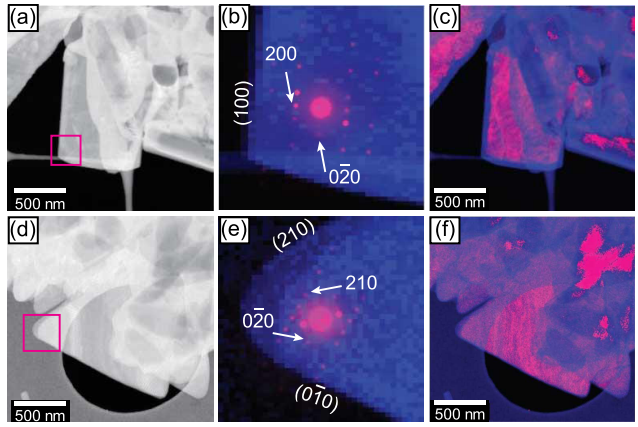

Figure 5. SED analysis of (a−c) ZnSe(ba) and (d−f) ZnSe(oa) exfoliated in EtOH. (a, d) Dark-field micrographs obtained by integration of scattering intensity. (b, e) Overlays of images (blue) and diffraction patterns (magenta) for selected regions marked in (a) and (d). The poles are marked with arrows on the diffraction patterns, and the corresponding surface planes are labeled on the images. (c, f) Overlays of images (blue) and crystallinity maps (magenta) formed by counting the Bragg peaks in diffraction patterns at each probe position.

assigned to (010)- and (210)-type planes (Figure 5d), where the direction in reciprocal space is aligned with the real space facet normal. By counting the number of Bragg peaks at each probe position,[41] a crystallinity map was created for ZnSe(ba) and ZnSe(oa) flakes (Figures 5c,f and S19c,f). The crystallinity maps enabled by SED reveal an approximately 50 nm layer along all edges containing no Bragg peaks for ZnSe(ba) flakes. In contrast, ZnSe(oa) flakes exhibit sharp alignment of the flake edge recorded in the overlaid image (blue) and the crystallinity map (magenta). Any loss of crystallinity of the same form as in ZnSe(ba) at the edge in ZnSe(oa) is therefore <8 nm in extent. Notably, loss of crystallinity at the edge was observed for both ZnSe(ba) and ZnSe(oa) flakes exfoliated in NMP (Figure S20). The approximately 50 nm layer exhibiting no Bragg peaks strongly indicates amorphization at the edges, concomitant with the oxidation at the flake edge observed by EELS (vide supra).

Both ligand and exfoliation solvent govern the degradation of exfoliated ZnSe(alkylamine). ZnSe(oa) exfoliated in EtOH exhibits limited oxidation and no loss of crystallinity at the flake edges. However, ligand selection alone does not preclude structural or chemical degradation given that ZnSe(oa) exfoliated in NMP exhibits comparable degradation to similarly exfoliated ZnSe(ba). Differences in faceting, or in this case edge termination, are well known to arise from differences in the thermodynamic or kinetic stability of crystal surfaces.[42] Here, the ZnSe(oa) flakes show a characteristic preference for (010) and (210) edges, whereas the ZnSe(ba) flakes consistently exhibit (010) and (100) edges. The common (010) edge termination constrains the role of the differences in facet energetics or kinetics since degradation, when observed, shows no preference for a particular facet. Consequently, the driving forces for a preferred edge termination encountered during exfoliation are significantly greater than those relevant to degradation. Small differences in flake thickness observed across exfoliated samples are also unlikely to play a significant role in the observed edge-based degradation. Cumulatively, ligand−solvent interactions during exfoliation determine the

https://dx.doi.org/10.1021/acs.chemmater.9b04800
Chem. Mater. 2020, 32, 2379−2388

ensuing degradation processes. Solvent removal of ligands likely introduces sites for enhanced oxidation, which then propagate from the flake surfaces. The oxidation of bulk ZnSe(alkylamine) illustrates that independent, slowly evolving degradation processes in air occur, as well as degradation during exfoliation in solvent. Selection of compatible solvent and alkylamine, as in the case of ZnSe(oa) and EtOH, provides a successful route to ZnSe(alkylamine) flakes of high compositional and structural quality with minimized exfoliation-associated degradation.

CONCLUSIONS

In summary, the morphological and chemical changes of two alkylamine II−VI LHs, ZnSe(ba) and ZnSe(oa), are scrutinized for the first time after shear exfoliation. Exfoliation down to bilayer flakes is demonstrated, and shear mixing produces dispersions having concentrations similar to those achieved by the shear exfoliation of graphite and MoS_2.

Analysis of the exfoliated material by Raman and X-ray photoelectron spectroscopies shows that these materials are not indefinitely stable in ambient conditions. Depending on processing parameters, the metal chalcogenide layer begins to convert to amorphous Se or crystalline h-Se and ZnO; exposure to ambient conditions facilitates this oxidative degradation. This chemical transformation is primarily governed by mechanical energy input during shear exfoliation, ligand−solvent interaction, and time of exposure to ambient conditions. Degradation is best mitigated by reducing shear rate, increasing the carbon chain length of the Zn-bound alkylamine (e.g., using oa instead of ba), and exfoliating from EtOH (among the solvents tested). SED also revealed local loss of crystallinity at flake edges for ZnSe(ba) EtOH, but not EtOH-exfoliated ZnSe(oa). Exfoliation from NMP led to extensive loss of flake edge crystallinity for both materials.

This work represents a comprehensive case study of the factors governing the exfoliation and stability of archetypal II−VI LHs. Given the versatility of this class of materials and their unique functional properties, this report highlights important factors that must be considered when processing II−VI LHs for incorporation into advanced (opto)electronic devices. Future work will focus on developing a clearer understanding of the chemical pathway(s) leading to LH degradation. We expect that, in analogy to what has been demonstrated in ZnSe quantum dots and nanoplatelets,[43] replacement of L-type alkylamine ligands with X-type ionic ligands may better stabilize LHs for solution processing.

MATERIALS AND METHODS

Materials. Zinc nitrate hexahydrate (99% trace-metal basis, Beantown Chemical), selenium powder (99%, Strem Chemicals), *n*-butylamine (99+%, Acros Organics), and *n*-octylamine (99+%, Sigma-Aldrich) were used without further purification. Organic solvents, including tetrahydrofuran (THF), *N*-methylpyrrolidone (NMP), ethanol (EtOH), ethylene glycol, and *N*,*N*-dimethylformamide (DMF), were purchased from Sigma-Aldrich, were of high-performance liquid chromatography (HPLC) grade, and were used without further purification.

Synthesis of ZnSe(ba). ZnSe(ba) was synthesized as described in a previous report.[8]

Synthesis of ZnSe(oa). ZnSe(oa) was synthesized by a ligand exchange reaction. ZnSe(ba) was synthesized as described previously.[8] After washing and drying, a dry powder (100 mg, 0.5 mmol) of ZnSe(ba) was dispersed in a large excess of oa (6 mL, 36 mmol). The mixture of ZnSe(ba) and oa was transferred to a Teflon-lined steel autoclave and incubated at 80 °C for 120 h. The final product was washed with 75% ethanol 3 times and stored in diethyl ether for further use.

Preparation of Exfoliated Dispersions of ZnSe(ba) and ZnSe(oa). THF, EtOH, DMF, NMP, ethylene glycol, and deionized water were selected as solvents to perform exfoliation. In a typical exfoliation experiment, using ZnSe(ba) as an example, ZnSe(ba) (20 mg, 0.10 mmol) was dispersed in 100 mL of solvent in a 200 mL Pyrex bottle. The ZnSe(ba)−solvent mixture was homogenized using a shear mixer (L5M-A, Silverson Machines, East Longmeadow) having a rotor diameter of 32 mm and equipped with a high shear screen at 6000 rpm for 1 h, exfoliating the ZnSe(ba). The dispersed, exfoliated material was divided into two aliquots and stored under ambient conditions until further use. ZnSe(oa) was exfoliated using the same preparation method, with 27 mg (0.10 mmol) of ZnSe(oa) added to 100 mL of solvent to form the mixture used for exfoliation. Our choice of these exfoliation parameters as a starting point was motivated by several factors. First, the evaporation rate of EtOH is significantly greater than that of more common exfoliation solvents such as NMP, allowing us to screen samples by AFM more rapidly at the early stages of our studies. Heating sample substrates to accelerate evaporation (in the case of NMP) was found to result in irreversible morphological changes. Second, these parameters led to exfoliated flake dispersion concentrations adequate for flake deposition on analysis substrates such as AFM substrates and TEM grids. Other exfoliation parameters were tested as well, as discussed in the Results and Discussion section.

Dispersion Concentration Measurements. First, calibration curves were obtained by dividing one previously prepared aliquot of exfoliated material (vide supra) into five separate fractions and diluting each respective fraction to a concentration of 0.2, 0.16, 0.12, 0.08, or 0.04 g/L. These diluted fractions were analyzed by UV−vis absorption spectroscopy (V-770, Jasco Inc., Easton) to construct Beer−Lambert concentration calibration curves. Calibration curves were measured in triplicate to ensure linearity and reproducibility. To measure the amount of dispersed material in solution after exfoliation, the second aliquot (35 mL) of solvent-dispersed ZnSe(ba) was transferred to a centrifuge tube and subject to centrifugation at 1500 rpm for 40 min to remove larger aggregates. After centrifugation, the top ∼10 mL of supernatant was removed and immediately analyzed by absorption spectroscopy to determine the dispersion concentration. These measurements were also repeated in triplicate.

Atomic Force Microscopy (AFM). To prepare samples for analysis by AFM, a 20 μL drop of supernatant, prepared after centrifugation as described above, containing dispersed ZnSe(ba) or ZnSe(oa), was spin-cast onto a 1 cm × 1 cm "ultraflat" silicon wafer with roughness less than 0.3 nm (product #21610-6, Ted Pella Inc., Altadena, CA) using a spin coater (Ossila Inc., Sheffield, England) at 1000 rpm for 5 min. The coated substrates were further dried under reduced pressure (∼1 Torr) at room temperature. All samples were analyzed by AFM in tapping mode using an MFP-3D Origin+ (Asylum Research, Boston) equipped with an ARC2 controller and a silicon probe (AC240TS-R3, Asylum Research, Boston) in air at room temperature. The AFM was calibrated by the manufacturer using micropatterned Si calibration standards.

Scanning Electron Microscopy (SEM). SEM imaging was conducted using an LEO 1550 SEM (Zeiss, Oberkochen, Germany) with a Schottky field emitter source at an accelerating voltage of 3 kV. A standard 30 μm aperture was used at a working distance of 3−6 mm with an InLens detector.

Transmission Electron Microscopy (TEM). Selected area electron diffraction (SAED) and bright-field imaging were carried out on a Tecnai F20 (Thermo Fisher) electron microscope equipped with a field emission gun electron source and a OneView camera (Gatan) operated at 200 kV. STEM, EELS, and X-ray EDS on all samples, as well as SAED and bright-field imaging on ZnSe(oa) exfoliated in EtOH, were carried out on an Osiris (Thermo Fisher) electron microscope operated at 80 kV and equipped with a high-brightness "X-FEG" electron source, an Enfinium dedicated energy loss spectrometer, and a "Super-X" EDS system consisting of four

https://dx.doi.org/10.1021/acs.chemmater.9b04800
Chem. Mater. 2020, 32, 2379−2388

silicon drift detectors mounted symmetrically about the optic axis. SAED and bright-field TEM imaging were obtained on a CCD camera mounted before the entrance aperture of the spectrometer. Spectroscopy data were processed in HyperSpy,[44] an open-source Python library.

Scanning electron diffraction (SED) was performed using a JEOL ARM300CF microscope at the Diamond Light Source, U.K., equipped with a cold field emission gun electron source and JEOL spherical aberration correctors in both the probe- and image-forming optics. The instrument was operated at 200 kV and aligned in an uncorrected nanobeam configuration with a 10 μm condenser aperture to obtain a convergence semiangle of approximately <1 mrad and a diffraction-limited probe diameter <5 nm. Diffraction patterns were acquired at each probe position on a Merlin-medipix direct electron detector, a counting type detector. A raster pattern consisting of 256 × 256 probe positions was recorded with diffraction patterns recorded on 256 × 256 pixels. The step between probe positions was 7.7 nm. The diffraction patterns were calibrated using a gold cross-grating reference consisting of SED collected under identical optical conditions on gold nanoparticles to obtain a polycrystalline ring pattern. The rotation between the real space image and the diffraction plane was calibrated using a MoO_3 reference sample. All SED data processing was carried out using pyXem, an open-source Python library.[45] Crystallinity maps were obtained by finding all Bragg scattering peaks in the diffraction pattern at each probe position using a difference of Gaussian method.

Raman Spectroscopy. Raman characterization was performed on both exfoliated ZnSe(ba) and ZnSe(oa) samples. Samples of exfoliated ZnSe(ba) and ZnSe(oa) were prepared by subjecting 30 mL of exfoliated material dispersion to centrifugation at 8000 rpm for 10 min. The resulting precipitate was further washed with EtOH 2 times before drying under reduced pressure (~1 Torr) at room temperature. Diethyl ether (2 mL) was introduced to disperse the sample again with mild vortex mixing for 1 min. Concentrated dispersion (20 μL) was then drop-cast on a 1 cm × 1 cm piece of Al foil and further dried under reduced pressure (~1 Torr). Data were collected with an inVia Raman microscope (Renishaw, West Dundee) using a 785 nm laser excitation wavelength. Laser power was adjusted to avoid sample damage.

Oxidation Measurement by UV−Vis Spectroscopy. The relative oxidation rates of ZnSe(ba) and ZnSe(oa) in air were measured using a Jasco V-770 UV−vis near-infrared (UV−vis−NIR) spectrophotometer equipped with an integrating sphere attachment (ISV-922, 60 mm sphere diameter). Dry ZnSe(ba) and ZnSe(oa) were dispersed onto Al foil (approximately 16 mm diameter). The samples were then placed into a powder cell (Jasco PSH-002, 16 mm diameter) for diffuse reflectance measurements. After each measurement, the sample was carefully returned to ambient conditions to prevent sample delamination from the Al foil.

Powder X-ray Diffraction (XRD). Powder X-ray diffractograms of bulk and exfoliated ZnSe(ba) and ZnSe(oa) were obtained with a D8 Advance X-ray powder diffractometer (Bruker Corp., Billerica) using Cu Kα radiation. Measurements were performed with a step size of 0.02° (2θ) at a rate of 0.2 s/step at room temperature. Samples of exfoliated ZnSe(ba) and ZnSe(oa) were prepared as described above and analyzed immediately after Raman spectroscopic analysis.

X-ray Photoelectron Spectroscopy (XPS). A PHI 5000 VersaProbe (ULVAC-PHI, Kanagawa, Japan) was used with a monochromatic Al Kα X-ray radiation source. The source power was 50 W and the pass energy was set to 117.4 eV for survey scans and 23.5 V for high-resolution scans. The time per step was 50 ms. CasaXPS (Casa Software, Ltd.) was used for data analysis.

Construction of Hypothetical Model of ZnSe(oa). Using ZnSe(ba)[8] as a template, a hypothetical model of ZnSe(oa) was constructed in Materials Studio 7.0 (Biovia, San Diego, CA). Carbon and hydrogen atoms were added to the end of the ba chains until the full length of the chain (eight carbon atoms) was reached. After replacing the ba chain with oa in this manner, the structure's geometry and unit cell parameters were optimized using Forcite, a force-field-based molecular mechanics module available in Materials Studio. For optimization, the Universal force field[46] was used with identical parameters as described previously.[47] The resulting geometry-optimized structure is shown in Figure 1a. Space group: *Pbca*. Unit cell parameters: *a*: 6.578531 Å; *b*: 5.982385 Å; *c*: 54.605749 Å; α: 90.000°; β: 90.000°; γ: 90.000°.

■ ASSOCIATED CONTENT

Supporting Information

The Supporting Information is available free of charge at https://pubs.acs.org/doi/10.1021/acs.chemmater.9b04800.

Schematic illustration of ZnSe(oa); additional SEM images; additional AFM images; layer thickness analysis by EELS; X-ray EDS; simulated electron diffraction patterns; additional Raman spectroscopy data; additional XPS data; additional EELS data; and additional SED data (PDF)

■ AUTHOR INFORMATION

Corresponding Author

Jeremy I. Feldblyum − *Department of Chemistry, The University at Albany, SUNY, Albany, New York 12222, United States*; orcid.org/0000-0001-6667-9587; Email: jfeldblyum@albany.edu

Authors

Mengwen Yan − *Department of Chemistry, The University at Albany, SUNY, Albany, New York 12222, United States*

Sean M. Collins − *School of Chemical and Process Engineering and School of Chemistry, University of Leeds, Leeds LS2 9JT, United Kingdom; Department of Materials Science and Metallurgy, University of Cambridge, Cambridge CB3 0FS, United Kingdom*; orcid.org/0000-0002-5151-6360

Paul A. Midgley − *Department of Materials Science and Metallurgy, University of Cambridge, Cambridge CB3 0FS, United Kingdom*

Complete contact information is available at: https://pubs.acs.org/10.1021/acs.chemmater.9b04800

Author Contributions

The manuscript was written through contributions of all authors. All authors have given approval to the final version of the manuscript.

Notes

The authors declare no competing financial interest.

■ ACKNOWLEDGMENTS

The authors gratefully acknowledge support from the Donors of the American Chemical Society Petroleum Research Fund (#59835-DNI10) and start-up funds provided by The University at Albany, State University of New York, in support of this work. S.M.C. acknowledges the support of a Henslow Research Fellowship at Girton College, Cambridge. P.A.M. acknowledges the Engineering and Physical Sciences Research Council, U.K. (EP/R008779/1). The authors acknowledge access and support in the use of the electron Physical Science Imaging Center (MG21980) at the Diamond Light Source, U.K. The authors thank S. Peczonczyk (Ford Motor Company), M. Lukatskaya (ETH Zürich), D. Genna (Youngstown State University), and R. Planty (Rensselaer Polytechnic Institute) for helpful discussions and technical support.

REFERENCES

(1) Novoselov, K. S.; Geim, A. K.; Morozov, S. V.; Jiang, D.; Zhang, Y.; Dubonos, S. V.; Grigorieva, I. V.; Firsov, A. A. Electric Field Effect in Atomically Thin Carbon Films. *Science* **2004**, *306*, 666−669.

(2) Chhowalla, M.; Shin, H. S.; Eda, G.; Li, L.-J.; Loh, K. P.; Zhang, H. The Chemistry of Two-Dimensional Layered Transition Metal Dichalcogenide Nanosheets. *Nat. Chem.* **2013**, *5*, 263.

(3) Pacilé, D.; Meyer, J. C.; Girit, ÇÖ.; Zettl, A. The Two-Dimensional Phase of Boron Nitride: Few-Atomic-Layer Sheets and Suspended Membranes. *Appl. Phys. Lett.* **2008**, *92*, No. 133107.

(4) Liu, H.; Neal, A. T.; Zhu, Z.; Luo, Z.; Xu, X.; Tománek, D.; Ye, P. D. Phosphorene: An Unexplored 2D Semiconductor with a High Hole Mobility. *ACS Nano* **2014**, *8*, 4033−4041.

(5) Dou, L.; Wong, A. B.; Yu, Y.; Lai, M.; Kornienko, N.; Eaton, S. W.; Fu, A.; Bischak, C. G.; Ma, J.; Ding, T.; Ginsberg, N. S.; Wang, L.-W.; Alivisatos, A. P.; Yang, P. Atomically Thin Two-Dimensional Organic-Inorganic Hybrid Perovskites. *Science* **2015**, *349*, 1518−1521.

(6) Mak, K. F.; Lee, C.; Hone, J.; Shan, J.; Heinz, T. F. Atomically Thin MoS_2: A New Direct-Gap Semiconductor. *Phys. Rev. Lett.* **2010**, *105*, No. 136805.

(7) Huang, X.; Li, J.; Fu, H. The First Covalent Organic−Inorganic Networks of Hybrid Chalcogenides: Structures That May Lead to a New Type of Quantum Wells. *J. Am. Chem. Soc.* **2000**, *122*, 8789−8790.

(8) Huang, X.; Li, J. From Single to Multiple Atomic Layers: A Unique Approach to the Systematic Tuning of Structures and Properties of Inorganic−Organic Hybrid Nanostructured Semiconductors. *J. Am. Chem. Soc.* **2007**, *129*, 3157−3162.

(9) Ki, W.; Li, J. A Semiconductor Bulk Material That Emits Direct White Light. *J. Am. Chem. Soc.* **2008**, *130*, 8114−8115.

(10) Fu, H.; Li, J. Density-Functional Study of Organic−Inorganic Hybrid Single Crystal $ZnSe(C_2H_8N_2)_{1/2}$. *J. Chem. Phys.* **2004**, *120*, 6721−6725.

(11) Huang, X.; Heulings, H. R.; Li, J.; Yuen, T.; Lin, C. L. Towards Dilute Magnetic Semiconductors: Fe and Co Substituted Inorganic-Organic Hybrid Materials Based on ZnSe. *J. Nanosci. Nanotechnol.* **2005**, *5*, 1487−1491.

(12) Wang, S.; Li, J. Two-Dimensional Inorganic−Organic Hybrid Semiconductors Composed of Double-Layered ZnS and Monoamines with Aromatic and Heterocyclic Aliphatic Rings: Syntheses, Structures, and Properties. *J. Solid State Chem.* **2015**, *224*, 40−44.

(13) Yao, Y.; DeKoster, G. T.; Buhro, W. E. Interchange of L-, Z-, and Bound-Ion-Pair X-Type Ligation on Cadmium Selenide Quantum Belts. *Chem. Mater.* **2019**, *31*, 4299−4312.

(14) Ithurria, S.; Tessier, M. D.; Mahler, B.; Lobo, R. P. S. M.; Dubertret, B.; Efros, A. L. Colloidal Nanoplatelets with Two-Dimensional Electronic Structure. *Nat. Mater.* **2011**, *10*, 936.

(15) Lesnyak, V.; George, C.; Genovese, A.; Prato, M.; Casu, A.; Ayyappan, S.; Scarpellini, A.; Manna, L. Alloyed Copper Chalcogenide Nanoplatelets via Partial Cation Exchange Reactions. *ACS Nano* **2014**, *8*, 8407−8418.

(16) Favron, A.; Gaufrès, E.; Fossard, F.; Phaneuf-L'Heureux, A.-L.; Tang, N. Y. W.; Lévesque, P. L.; Loiseau, A.; Leonelli, R.; Francoeur, S.; Martel, R. Photooxidation and Quantum Confinement Effects in Exfoliated Black Phosphorus. *Nat. Mater.* **2015**, *14*, 826.

(17) Yi, M.; Shen, Z. A Review on Mechanical Exfoliation for the Scalable Production of Graphene. *J. Mater. Chem. A* **2015**, *3*, 11700−11715.

(18) Shim, J.; Bae, S.-H.; Kong, W.; Lee, D.; Qiao, K.; Nezich, D.; Park, Y. J.; Zhao, R.; Sundaram, S.; Li, X.; Yeon, H.; Choi, C.; Kum, H.; Yue, R.; Zhou, G.; Ou, Y.; Lee, K.; Moodera, J.; Zhao, X.; Ahn, J.-H.; Hinkle, C.; Ougazzaden, A.; Kim, J. Controlled Crack Propagation for Atomic Precision Handling of Wafer-Scale Two-Dimensional Materials. *Science* **2018**, *362*, 665−670.

(19) Jawaid, A.; Che, J.; Drummy, L. F.; Bultman, J.; Waite, A.; Hsiao, M.-S.; Vaia, R. A. Redox Exfoliation of Layered Transition Metal Dichalcogenides. *ACS Nano* **2017**, *11*, 635−646.

(20) Kovtyukhova, N. I.; Wang, Y.; Berkdemir, A.; Cruz-Silva, R.; Terrones, M.; Crespi, V. H.; Mallouk, T. E. Non-Oxidative Intercalation and Exfoliation of Graphite by Brønsted Acids. *Nat. Chem.* **2014**, *6*, 957.

(21) Tanaka, T.; Ebina, Y.; Takada, K.; Kurashima, K.; Sasaki, T. Oversized Titania Nanosheet Crystallites Derived from Flux-Grown Layered Titanate Single Crystals. *Chem. Mater.* **2003**, *15*, 3564−3568.

(22) Sun, Y.; Sun, Z.; Gao, S.; Cheng, H.; Liu, Q.; Piao, J.; Yao, T.; Wu, C.; Hu, S.; Wei, S.; Xie, Y. Fabrication of Flexible and Freestanding Zinc Chalcogenide Single Layers. *Nat. Commun.* **2012**, *3*, No. 1057.

(23) Tao, H.; Zhang, Y.; Gao, Y.; Sun, Z.; Yan, C.; Texter, J. Scalable Exfoliation and Dispersion of Two-Dimensional Materials−An Update. *Phys. Chem. Chem. Phys.* **2017**, *19*, 921−960.

(24) Paton, K. R.; Varrla, E.; Backes, C.; Smith, R. J.; Khan, U.; O'Neill, A.; Boland, C.; Lotya, M.; Istrate, O. M.; King, P.; Higgins, T.; Barwich, S.; May, P.; Puczkarski, P.; Ahmed, I.; Moebius, M.; Pettersson, H.; Long, E.; Coelho, J.; O'Brien, S. E.; McGuire, E. K.; Sanchez, B. M.; Duesberg, G. S.; McEvoy, N.; Pennycook, T. J.; Downing, C.; Crossley, A.; Nicolosi, V.; Coleman, J. N. Scalable Production of Large Quantities of Defect-Free Few-Layer Graphene by Shear Exfoliation in Liquids. *Nat. Mater.* **2014**, *13*, 624.

(25) Varrla, E.; Backes, C.; Paton, K. R.; Harvey, A.; Gholamvand, Z.; McCauley, J.; Coleman, J. N. Large-Scale Production of Size-Controlled MoS_2 Nanosheets by Shear Exfoliation. *Chem. Mater.* **2015**, *27*, 1129−1139.

(26) Egerton, R. F. *Electron Energy-Loss Spectroscopy in the Electron Microscope*, 3rd ed.; Springer: New York, 2011.

(27) Iakoubovskii, K.; Mitsuishi, K.; Nakayama, Y.; Furuya, K. Thickness Measurements with Electron Energy Loss Spectroscopy. *Microsc. Res. Tech.* **2008**, *71*, 626−631.

(28) Good, R. J. A Thermodynamic Derivation of Wenzel's Modification of Young's Equation for Contact Angles; Together with a Theory of Hysteresis1. *J. Am. Chem. Soc.* **1952**, *74*, 5041−5042.

(29) Hernandez, Y.; Lotya, M.; Rickard, D.; Bergin, S. D.; Coleman, J. N. Measurement of Multicomponent Solubility Parameters for Graphene Facilitates Solvent Discovery. *Langmuir* **2010**, *26*, 3208−3213.

(30) Manna, K.; Huang, H.-N.; Li, W.-T.; Ho, Y.-H.; Chiang, W.-H. Toward Understanding the Efficient Exfoliation of Layered Materials by Water-Assisted Cosolvent Liquid-Phase Exfoliation. *Chem. Mater.* **2016**, *28*, 7586−7593.

(31) Bang, G. S.; Nam, K. W.; Kim, J. Y.; Shin, J.; Choi, J. W.; Choi, S.-Y. Effective Liquid-Phase Exfoliation and Sodium Ion Battery Application of MoS_2 Nanosheets. *ACS Appl. Mater. Interfaces* **2014**, *6*, 7084−7089.

(32) Sabine, T. M.; Hogg, S. The Wurtzite Z Parameter for Beryllium Oxide and Zinc Oxide. *Acta Crystallogr., Sect. B: Struct. Crystallogr. Cryst. Chem.* **1969**, *25*, 2254−2256.

(33) Bradley, A. J. L. The Crystal Structures of the Rhombohedral Forms of Selenium and Tellurium. *London Edinburgh Philos. Mag. J. Sci.* **1924**, *48*, 477−496.

(34) Ren, L.; Zhang, H.; Tan, P.; Chen, Y.; Zhang, Z.; Chang, Y.; Xu, J.; Yang, F.; Yu, D. Hexagonal Selenium Nanowires Synthesized via Vapor-Phase Growth. *J. Phys. Chem. B* **2004**, *108*, 4627−4630.

(35) Nagels, P.; Sleeckx, E.; Callaerts, R.; Tichy, L. Structural and Optical Properties of Amorphous Selenium Prepared by Plasma-Enhanced CVD. *Solid State Commun.* **1995**, *94*, 49−52.

(36) Yang, K.; Cui, Q.; Hou, Y.; Liu, B.; Zhou, Q.; Hu, J.; Mao, H.-K.; Zou, G. Pressure-Induced Crystallization and Phase Transformation of Amorphous Selenium: Raman spectroscopy and X-Ray Diffraction Studies. *J. Phys.: Condens. Matter* **2007**, *19*, No. 425220.

(37) Shirley, D. A. High-Resolution X-Ray Photoemission Spectrum of the Valence Bands of Gold. *Phys. Rev. B* **1972**, *5*, 4709−4714.

(38) Wang, D.; Chang, Y.-L.; Liu, Z.; Dai, H. Oxidation Resistant Germanium Nanowires: Bulk Synthesis, Long Chain Alkanethiol Functionalization, and Langmuir−Blodgett Assembly. *J. Am. Chem. Soc.* **2005**, *127*, 11871−11875.

(39) Eggeman, A. S. Scanning Transmission Electron Diffraction Methods. *Acta Crystallogr., Sect. B: Struct. Sci., Cryst. Eng. Mater.* **2019**, *75*, 475−484.

https://dx.doi.org/10.1021/acs.chemmater.9b04800
Chem. Mater. 2020, 32, 2379−2388

(40) Ophus, C. Four-Dimensional Scanning Transmission Electron Microscopy (4D-STEM): From Scanning Nanodiffraction to Ptychography and Beyond. *Microsc. Microanal.* **2019**, *25*, 563−582.
(41) Hou, J.; Ashling, C. W.; Collins, S. M.; Krajnc, A.; Zhou, C.; Longley, L.; Johnstone, D. N.; Chater, P. A.; Li, S.; Coulet, M.-V.; Llewellyn, P. L.; Coudert, F.-X.; Keen, D. A.; Midgley, P. A.; Mali, G.; Chen, V.; Bennett, T. D. Metal-Organic Framework Crystal-Glass Composites. *Nat. Commun.* **2019**, *10*, No. 2580.
(42) Ringe, E.; Van Duyne, R. P.; Marks, L. D. Kinetic and Thermodynamic Modified Wulff Constructions for Twinned Nanoparticles. *J. Phys. Chem. C* **2013**, *117*, 15859−15870.
(43) Owen, J. The Coordination Chemistry of Nanocrystal Surfaces. *Science* **2015**, *347*, 615−616.
(44) De la Peña, F.; Ostasevicius, T.; Tonaas Fauske, V.; Burdet, P.; Jokubauskas, P.; Nord, M.; Prestat, E.; Sarahan, M.; MacArthur, K. E.; Johnstone, D. N.; Taillon, J.; Caron, J.; Furnival, T.; Eljarrat, A.; Mazzucco, S.; Migunov, V.; Aarholt, T.; Walls, M.; Winkler, F.; Martineau, B.; Donval, G.; Hoglund, E. R.; Alxneit, I.; Hjorth, I.; Zagonel, L. F.; Garmannslund, A.; Gohlke, C.; Iyengar, I.; Chang, H.-W. *HyperSpy/HyperSpy: HyperSpy v1.31*; Zenodo: Geneva, Switzerland, 2018.
(45) Johnstone, D. N.; Crout, P.; Høgås, S.; Martineau, B.; Laulainen, J.; Collins, S.; Smeets, S.; Morzy, J.; Prestat, E.; Doherty, T.; Ostasevicius, T.; Bergh, T.; Ånes, H. *pyXem*, v0.8.0; Zenodo: Geneva, Switzerland, 2019.
(46) Caglioti, G.; Paoletti, A.; Ricci, F. P. Choice of Collimators for a Crystal Spectrometer for Neutron Diffraction. *Nucl. Instrum.* **1958**, *3*, 223−228.
(47) Feldblyum, J. I.; McCreery, C. H.; Andrews, S. C.; Kurosawa, T.; Santos, E. J.; Duong, V.; Fang, L.; Ayzner, A. L.; Bao, Z. Few-Layer, Large-Area, 2D Covalent Organic Framework Semiconductor Thin Films. *Chem. Commun.* **2015**, *51*, 13894−13897.

https://dx.doi.org/10.1021/acs.chemmater.9b04800
Chem. Mater. 2020, 32, 2379−2388